Strong confinement-induced nonlinear terahertz response in semiconductor nanostructures revealed by Monte Carlo calculations

Jiří Kuchařík and Hynek Němec *
Institute of Physics ASCR, Na Slovance 2, 182 21 Prague 8, Czech Republic

(Received 31 July 2019; revised 13 May 2021; accepted 14 May 2021; published 27 May 2021)

Nonlinear terahertz conductivity spectra of charges confined in semiconductor nanostructures were calculated using a semiclassical Monte Carlo method. The confinement-induced nonlinear response per charge carrier is much stronger than the intrinsic nonlinearity of common bulk semiconductors and more than 20 times stronger than in graphene, which has been considered as a material with one of the highest terahertz nonlinearities. Moderate intensities of the terahertz radiation are thus sufficient to achieve efficient frequency mixing or high-harmonics generation. Enclosing the nanostructures into metallic nanoslits concentrates the electric field into the semiconductor and thus easily provides nonlinear terahertz signal strength comparable to the linear one.

DOI: 10.1103/PhysRevB.103.205426

I. INTRODUCTION

Nonlinear response of solids to radio waves has been known for more than a century; for example, the rectifying properties of a contact between a mineral and a metal have been utilized in crystal radios. The development of laser technologies has led to the investigation and exploitation of nonlinear processes at optical and infrared frequencies, including generation of harmonic frequencies, frequency mixing, or parametric amplification [1]. While linear response of materials is well understood in a broad spectral range including the terahertz (THz) range [2–5], nonlinear properties of solids are less known, and their knowledge in the THz range is particularly limited.

The new sources (including table-top devices based on tilted-wavefront optical rectification in $LiNbO_3$ [6] or large-scale facilities such as free electron lasers [7]) generate THz pulses intense enough to *control* material properties—the induced changes are typically monitored using optical pulses [8]. However, investigations of *nonlinear* THz properties have been mostly limited to band transport in bulk semiconductors [9]; these include THz-pulse-induced intervalley electron scattering and intravalley dynamics [10] and THz-induced interband tunneling of electrons [11]. Band transport is also the basis of high-harmonic generation by hot Dirac fermions in graphene [12]. Although quantum confinement proved useful for enhancing the nonlinearities at optical frequencies and for the discovery of new physical effects [13], almost no attention has been devoted to high-field transport and nonlinear conductivity of charges confined in semiconductor *nanostructures* in the *THz* frequency range. Strong nonlinearities are essential for application of nonlinear phenomena in table top devices, where only moderate intensities of terahertz radiation are available.

Here we develop a closed formalism enabling calculation of the experimentally observable signal from microscopic parameters. The key element is a semiclassical theory of nonlinear THz response of photogenerated confined charges. We first analyze the current induced by a THz electric field locally applied to a semiconductor nano-object: We show that a strong nonlinear response is associated with the charge confinement. Subsequently, effective medium theory is formulated to determine the effective nonlinear THz response of an ensemble of nano-objects in a macroscopic sample; more specifically, we investigate the photoconductivity of a periodic array of GaAs nanobars [Fig. 1(a)]. Since nano-objects in most structures are separated by air gaps or by a low-permittivity vehicle, there is a high dielectric contrast between the constituents, which is responsible for depolarization fields screening the applied THz field. We demonstrate that the field reduction inside the nano-objects suppresses the nonlinear effects so severely that it impedes a direct experimental observation of the output nonlinear signal. The full potential of the strong confinement-induced nonlinearity can be exploited using metallic nanoslits: These concentrate the THz field into the semiconductor nanostructure and therefore a strong nonlinear signal with intensity comparable to that of the linear signal is generated.

II. MONTE CARLO CALCULATIONS AND THEIR ANALYSIS

We implemented calculations based on a semiclassical Monte Carlo method simulating the thermal motion of photogenerated charges, following the scheme described in detail in Ref. [14]. In brief, charges undergo a Newtonian motion under the influence of a monochromatic electric field $E\cos(\omega t)$ (E is the field amplitude inside the nanobars). Within the applied Drude approximation, this motion is interrupted by scattering events occurring randomly with the mean time τ_s; the scattered velocity follows the Maxwell-Boltzmann statistical

*Corresponding author: nemec@fzu.cz

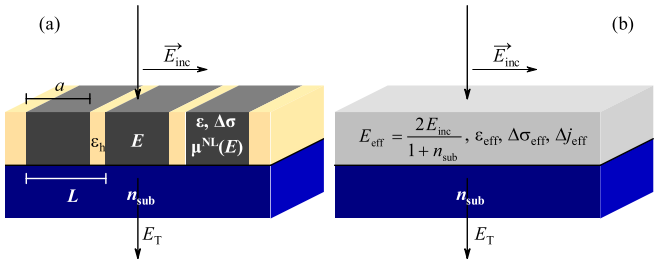

FIG. 1. (a) Scheme of the investigated nanostructure consisting of nanobars (dark gray) attached to a substrate. The THz field E_{inc} incident on the structure from the top is polarized perpendicularly to the nanobar axis; the filling factor s equals a/L. (b) Using a brick-wall effective medium approximation, the layer containing the nanobars separated by a material with permittivity ε_h is transformed into an equivalent homogeneous layer with effective properties.

distribution. We assume that charges are reflected back coherently when they reach the nanobar boundary.

The principal output is a time-dependent carrier mean velocity $v(t)$:

$$v(t) = \frac{1}{M}\sum_{j=1}^{M} v_j(t), \tag{1}$$

where $v_j(t)$ is the set of M simulated velocities of individual charges (typically we simulate up to $M = 4 \times 10^6$ trajectories for lower electric fields). Since the mean velocity in the thermal equilibrium and without an electric field is zero, the calculated mean velocity $v(t)$ in the presence of an electric field coincides with the mean drift velocity of charges. Unlike the Kubo-formula-based calculations [15], this method inherently accepts arbitrary electric field strengths and it is thus suitable also for the investigation for nonlinear phenomena.

The principal challenge associated with the nonlinear response consists in the analysis of the mean drift velocity $v(t)$, which no longer oscillates solely on the single driving frequency ω. In the stationary regime, higher harmonic frequencies may emerge, and a complex dependence on the electric field amplitude may be observed. In order to capture these two aspects, we will introduce two representations of the carrier mobility:

(i) A generalized field-dependent carrier mobility $\mu^{[\alpha]}(E)$ describing the generation of the αth-harmonic frequency $\alpha\omega$ (α is an integer).

(ii) A nonlinear mobility $\mu^{(n)}$ [analogical to nonlinear susceptibility $\chi^{(n)}$ in optics] describing the nth-order nonlinear process (velocity scaling with E^n).

In this paper, we prefer to concentrate on the single-carrier response (the mobility) of charges since it—in our opinion—best illustrates the potential for a strong nonlinear response. The collective response in the developed formalism scales with the carrier density and formulas analogical to the linear response remain valid. In particular, the nonlinear and harmonic conductivities read

$$\Delta\sigma^{(n)} = e_0 N \mu^{(n)} \quad \text{and} \quad \Delta\sigma^{[\alpha]} = e_0 N \mu^{[\alpha]}, \tag{2}$$

where N is the (photoexcited) carrier density and e_0 is the elementary charge. Important are also the nonlinear and harmonic susceptibilities which directly connect the developed calculations to the nonlinear polarization commonly employed in the field of nonlinear optics:

$$\chi^{[\alpha]} = \frac{\Delta\sigma^{[\alpha]}}{\alpha\omega\varepsilon_0} = \frac{e_0 N \mu^{[\alpha]}}{\alpha\omega\varepsilon_0}, \tag{3}$$

and

$$\chi^{(n)}(\dots) = \frac{\Delta\sigma^{(n)}(\dots)}{\alpha\omega\varepsilon_0} = \frac{e_0 N \mu^{(n)}(\dots)}{\alpha\omega\varepsilon_0}, \tag{4}$$

where "..." abbreviate the argument $\underbrace{\pm\omega \pm \omega \pm \dots}_{n\times} \to \alpha\omega$.

A. Generalized mobility $\mu^{[\alpha]}$

The carrier drift velocity $v(t)$ in the stationary regime can be decomposed into the harmonic series

$$v(t) = \mathrm{Re}\sum_{\alpha=0}^{\infty} \mu^{[\alpha]}(\alpha\omega, E) E e^{i\alpha\omega t}, \tag{5}$$

which expresses that an electric field with frequency ω produces oscillations at harmonic frequencies $\alpha\omega$. The coefficients $\mu^{[\alpha]}(\alpha\omega)$ represent the (complex) amplitudes of the velocity of charge oscillations at frequencies $\alpha\omega$ normalized by the electric field amplitude. These generalized mobilities are analogous to the charge mobility (including the same physical dimension) and they generally depend on the driving field E (for brevity, we will omit this dependence in the notation). In purely linear materials, no frequency mixing occurs and the series (5) contains a single term $\mu^{[1]}(\omega)$ coinciding with the standard linear mobility spectrum.

The generalized mobilities can be calculated straightforwardly, either using a Fourier analysis, or by linear regression. Since the basis functions are orthogonal, the procedure is stable, insensitive to numerical errors, and the retrieved coefficients are not influenced by the number of terms taken into account.

B. Nonlinear mobility $\mu^{(n)}$

To assess the nonlinearity strength, we decompose the carrier drift velocity v into a linear and a nonlinear component:

$$v = v^{\mathrm{L}} + v^{\mathrm{NL}} = \mu^{\mathrm{L}} E + \underbrace{\mu^{(3)}E^3 + \mu^{(5)}E^5 + \dots}_{\mu^{\mathrm{NL}}(E)\cdot E}. \tag{6}$$

Here μ^{L} is the linear charge carrier mobility, and $\mu^{\mathrm{NL}}(E)$ is the nonlinear field-dependent contribution to the mobility which can be expanded into powers of the field amplitude for weaker fields (even powers are symmetry forbidden in the investigated structure). The nonlinear mobilities $\mu^{(n)}$ are analogous to the nth-order susceptibilities $\chi^{(n)}$ representing nonlinear polarization in optics [Eq. (4)].

Each nonlinear mobility $\mu^{(n)}$ involves several processes; for example, $\mu^{(3)}$ involves third-harmonics generation $\mu^{(3)}(\omega + \omega + \omega \to 3\omega)$ as well as the parametric process $\mu^{(3)}(\omega + \omega - \omega \to \omega)$. Precisely speaking, the symbolic Eq. (6) thus represents a set of equations for distinct frequency

components:

$$\begin{aligned}
v(\omega) &= \mu^{\mathrm{L}}E + \tfrac{3}{4}\mu^{(3)}(\omega+\omega-\omega\to\omega)E^3 + \tfrac{10}{16}\mu^{(5)}(\omega+\omega+\omega-\omega-\omega\to\omega)E^5+\ldots \equiv \mu^{[1]}(\omega,E)E\\
v(3\omega) &= \tfrac{1}{4}\mu^{(3)}(\omega+\omega+\omega\to 3\omega)E^3 + \tfrac{5}{16}\mu^{(5)}(\omega+\omega+\omega+\omega-\omega\to 3\omega)E^5+\ldots \equiv \mu^{[3]}(3\omega,E)E\\
v(5\omega) &= \tfrac{1}{16}\mu^{(5)}(\omega+\omega+\omega+\omega+\omega\to 5\omega)E^5+\ldots \equiv \mu^{[5]}(5\omega,E)E\\
&\vdots \qquad\qquad \vdots \qquad\qquad \vdots\\
v(\alpha\omega) &= \textstyle\sum_{n=\alpha}^{\infty} C_{\alpha,n}\mu^{(n)}E^n \equiv \mu^{[\alpha]}(\alpha\omega,E)E.
\end{aligned} \tag{7}$$

These equations describe the transformation between the harmonic mobilities $\mu^{[\alpha]}$ and nonlinear mobilities $\mu^{(n)}$. The coefficients $C_{\alpha,n}$ reflect the degeneracy of the corresponding nonlinear processes [1]; in our case, only odd α and n contribute for which

$$C_{\alpha,n} = \frac{1}{2^{n-1}}\binom{n}{\frac{n-\alpha}{2}}. \tag{8}$$

In principle, the coefficients $\mu^{(n)}$ in each line of Eq. (7) (i.e., for each harmonic frequency) can be determined using a linear regression. However, for weaker electric fields, the corresponding design matrix is inevitably ill conditioned. Using higher electric fields is not an option, since higher-order nonlinear processes then become important, thus inflating the size of the design matrix leading to worse ill conditioning. In practice, third- or fifth-order nonlinear mobilities can be determined reliably, but higher-order effects require excessive amount of computation time to reduce the inherent statistical errors in the Monte Carlo method.

C. Calculated generalized mobility spectra

Examples of the generalized mobility spectra $\mu^{[\alpha]}(\alpha\omega)$ are shown in Fig. 2 (see also Fig. 7 in Appendix A). For all fields, the mobility amplitude at the fundamental frequency $|\mu^{[1]}|$ increases with frequency and reaches a broad maximum; then it decreases back toward zero due to the inertia of charges, analogically to the Drude formula. For the lowest fields ($E \leqslant 3$ kV/cm), the spectrum coincides with the linear mobility spectrum of confined charges [14,15]: The maximum at frequency f_0 reflects bouncing of the charges moving with the mean thermal velocity [15] and the broadness of the maximum stems from the broad distribution of thermal velocities in the Maxwell-Boltzmann statistics [16]. With increasing driving field amplitude, the mean velocity of charges increases; this increases also their bouncing frequency, thus causing the observed blue-shift of the peak frequency (inset in Fig. 2). Since the thermal and drift velocities are uncorrelated, squares of their mean values add together, therefore the peak position f_{peak} approximately follows $f_0\sqrt{1+(E/E_{\mathrm{therm}})^2}$ [the characteristic electric field E_{therm} is of the order of the field $k_BT/(e_0a)$ providing charges with the kinetic energy equal to their thermal energy]. The amplitude of the spectrum decreases with increasing E due to the transfer of energy into higher harmonics.

According to the Miller's rule [17], the αth-harmonic frequency generation can be viewed as a sequence of α first-order processes, and therefore the generalized mobility $|\mu^{[\alpha]}(\alpha\omega)|$ should be proportional to $|\mu^{[1]}(\omega)|^{\alpha}$. The spectra of $|\mu^{[\alpha]}(\alpha\omega)|$ (Fig. 2) indeed resemble this rough approximation: They exhibit a single broad band which narrows with increasing α as a consequence of the αth power, and their peak also blue-shifts with increasing field due to the increasing mean velocity. The amplitudes $|\mu^{[\alpha]}(\alpha\omega)|$ initially increase as $E^{\alpha-1}$ indicating the dominance of the αth-order nonlinear process. For more intense fields, higher-order processes (like $\omega+\omega-\omega\to\omega$ or $\omega+\omega+\omega-\omega-\omega\to\omega$ for $\alpha=1$) become important, causing the peak value to saturate and finally even decrease (see also Fig. 3). The early onset of these higher-order processes indicates that the motion of charges in a rectangular potential is a strongly field-dependent phenomenon even for moderate field amplitudes, thus allowing an efficient high-harmonics generation (Fig. 3). For example, as estimated from the ratio $|\mu^{[15]}(15\omega)/\mu^{[1]}(1\omega)|$, the 15th harmonic reaches almost 1% of the linear response at only 50 kV/cm. Har-

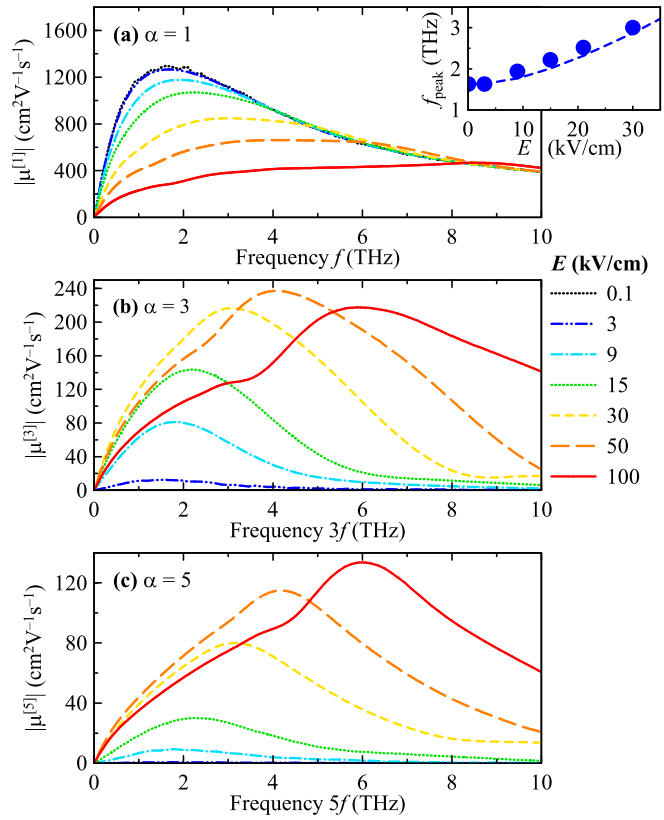

FIG. 2. [(a)–(c)] Examples of the spectra of amplitudes of generalized mobilities $\mu^{[\alpha]}$ for 100 nm wide GaAs nanobars ($m_{\mathrm{eff}} = 0.07m_e$, $\tau_s = 100$ fs) at room temperature. Inset: Frequency of the maximum in $|\mu^{[1]}|$ (symbols) and the trend discussed in the main text (dashed line).

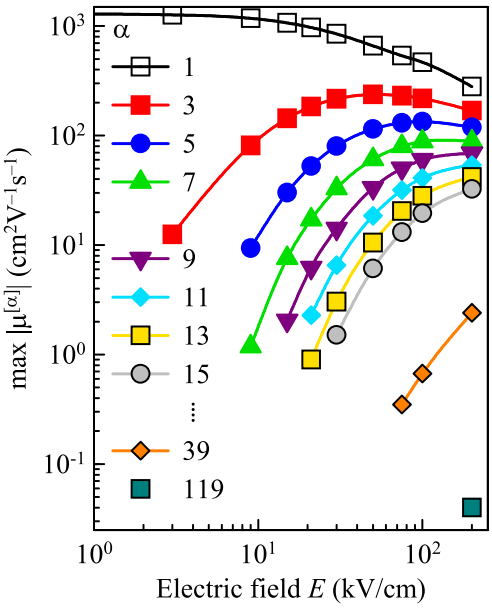

FIG. 3. Peak values of amplitudes of generalized mobilities spectra describing the generation of harmonics. For graphical clarity, only two selected high harmonics ($\alpha = 39$ and $\alpha = 119$) are included in the plot.

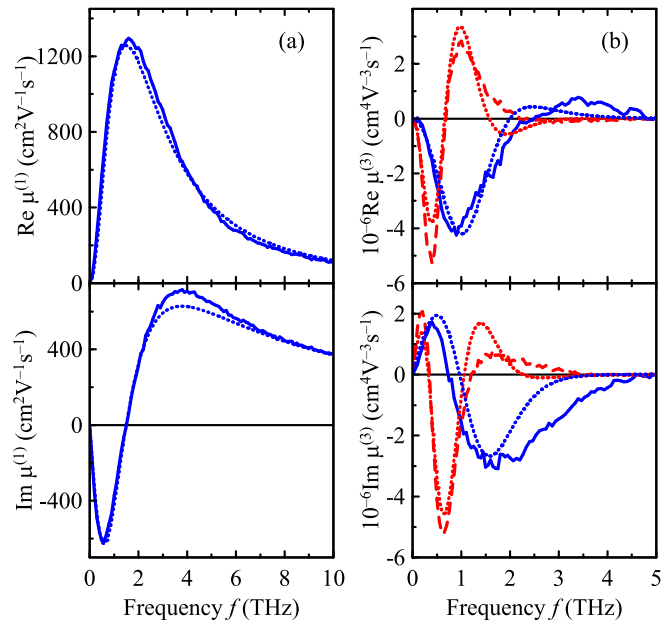

FIG. 4. Examples of complex (a) first- and (b) third-order nonlinear mobility spectra for the 100-nm-wide GaAs nanobars.

monics as high as 119 have been resolved in our Monte Carlo calculations for an extreme field of $E = 200$ kV/cm.

For intense electric fields, distinct shoulders start to develop in the spectra of $|\mu^{[\alpha]}(\alpha\omega)|$ below the main peak. These represent the contributions of the higher-order nonlinear processes. For example, the generalized mobility $\mu^{[3]}$ describes the third-harmonic generation through any nonlinear process. Its spectrum thus involves a superposition of nonlinear mobilities $\mu^{(3)}(\omega+\omega+\omega \to 3\omega)$, $\mu^{(5)}(\omega+\omega+\omega+\omega-\omega \to 3\omega)$, and higher. For low fields, the $\mu^{(3)}(\omega+\omega+\omega \to 3\omega)$ process dominates and the resulting response thus resembles $[\mu^{(1)}(\omega/3)]^3$ according to the Miller's rule. Indeed, a single peak is observed and it blue-shifts in the same way as the broad peak in $\mu^{(1)}$. For stronger fields, the contribution of the $\mu^{(5)}(\omega+\omega+\omega+\omega-\omega \to 3\omega)$ process becomes important; according to the Miller's rule, the spectrum of this contribution is proportional to $[\mu^{(1)}(\omega/5)]^5$. It is the different scaling of the frequency argument which causes the presence of the prominent shoulder in the $|\mu^{[3]}|$ spectrum. Similar arguments apply also for other generalized mobilities $\mu^{[\alpha]}$. Note that also the generalized mobility $\mu^{[1]}$ representing the response at the fundamental frequency involves linear mobility $\mu^{(1)}(\omega)$ as well as higher-order nonlinear processes $\mu^{(3)}(\omega+\omega-\omega \to 1\omega)$, $\mu^{(5)}(\omega+\omega+\omega-\omega-\omega \to 1\omega)$, etc.; indeed, small waves indicating the presence of these further processes can be resolved in the spectrum of $\mu^{[1]}$ for the highest field of 100 kV/cm [Fig. 2(a)].

D. Calculated nonlinear mobility spectra

Examples of decomposition of the calculated trajectory into the nonlinear mobility spectra are shown in Fig. 4. The first-order mobility spectrum $\mu^{(1)}$ coincides with the linear response of the structure, which can be (at least for narrower nanobars) well described using a simple oscillator model, $\mu^{(1)}(\omega) \propto i\omega/D(\omega)$, where $D(\omega) = \omega_{\rm osc}^2 - \omega^2 - i\omega\gamma$ [15].

The spectral shape becomes more complex for higher-order mobilities; notably, new lobes develop with the increasing nonlinear order n. This behavior can be qualitatively understood in the framework of the anharmonic oscillator model described in detail in Ref. [1]. For a weak anharmonicitiy [described by the potential $V(x) \propto \omega_{\rm osc}^2 x^2 + bx^4$] and not-too-strong electric fields, the nonlinear mobilities can be determined using the perturbation calculus:

$$\mu^{(3)}(\omega+\omega+\omega \to 3\omega) \propto \frac{i\omega}{D(3\omega)D^3(\omega)}, \tag{9}$$

$$\mu^{(3)}(\omega+\omega-\omega \to \omega) \propto \frac{i\omega}{D^3(\omega)D(-\omega)}. \tag{10}$$

Although a minor adjustment of the oscillator eigenfrequency $\omega_{\rm osc}$ is needed, this extraordinarily simple model is still capable to well reproduce the shape of the nonlinear mobility spectra. We verified that similar procedure works also for the fifth-order mobility and we assume that applicability is preserved also for higher orders.

For simplicity, we now focus on the third-harmonic generation and particularly on the behavior of the nonlinear mobility $\mu^{(3)}(\omega+\omega+\omega \to 3\omega)$. The nonlinear part $\mu^{\rm NL}$ of the mobility initially increases quadratically with the field [Fig. 5(a)], due to the dominance of the canonical third-order nonlinear process $\mu^{(3)}(\omega+\omega+\omega \to 3\omega)$. The departure from the parabola becomes important already for low fields (<10 kV/cm), indicating a significant role of higher-order nonlinear processes such as the $\mu^{(5)}$-process $\omega+\omega+\omega+\omega-\omega \to 3\omega$ [notice the contrast with the harmonic series (5) where the coefficients $\mu^{[\alpha]}$ represent a mixture of processes of the order $\mu^{(\alpha)}$ and higher]. Finally, the nonlinear mobility saturates at a value exceeding even that of the linear component.

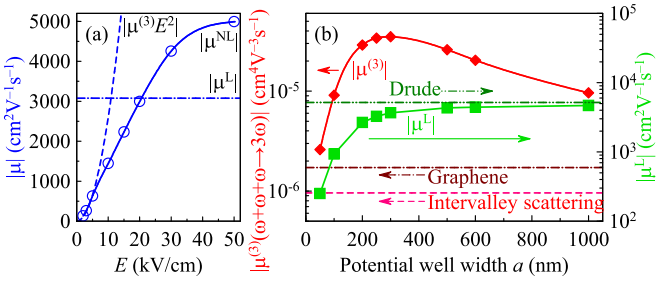

FIG. 5. (a) Amplitude of linear and nonlinear mobility components of charges confined in 500 nm wide GaAs nanobars (response to the local electric field). Dashed line: Quadratic fit of the nonlinear mobility at the three lowest electric fields, serving for the determination of the nonlinear mobility coefficient $\mu^{(3)}$. (b) Amplitude of the linear mobility and of the nonlinear mobility coefficient $\mu^{(3)}$ as a function of confinement length. Parameters of Monte Carlo calculations: $m_{\text{eff}} = 0.07m_e$, $\tau_s = 270$ fs (high-quality GaAs at room temperature), driving frequency 0.5 THz. For convenience, the magnitude of the Drude mobility in bulk GaAs is indicated together with the nonlinear mobility coefficients associated with intervalley scattering in GaAs and with electronic response of graphene, as estimated in the main text.

At a fixed frequency, the *linear* mobility amplitude $|\mu^{\text{L}}|$ increases with increasing confinement length [Fig. 5(b)]: Charges interact less with the nanobar boundaries, thus reducing the effective scattering [15]. For the same reason, the *nonlinear* mobility increases for narrow nanobars, too. However, the nonlinearities are induced solely by the charge confinement in our model, therefore the nonlinear response vanishes for infinite confinement length. The maximum in between is broad, reaching $|\mu^{(3)}(\omega+\omega+\omega\rightarrow3\omega)| \approx 35\times10^{-6}$ cm^4 V^{-3} s^{-1}.

We now compare this value to nonlinearities originating from other physical mechanisms (these levels are also indicated in Fig. 5).

Hebling *et al.* investigated absorption bleaching due to scattering of electrons into side valleys with smaller mobility [10]. Since absorption coefficient α is connected to the conductivity as $\sigma = n\varepsilon_0 c\alpha$ (c is the light velocity in vacuum and $n = 3.56$ is the THz refractive index of GaAs), we get from Eq. (2) the field-dependent mobility $\mu(E)$ [the concentration N in Eq. (2) is the doping density in this case]. A quadratic fit of the $\mu(E)$ dependence then provides the estimate for the third-order nonlinear coefficient $|\mu^{(3)}(\omega+\omega+\omega\rightarrow3\omega)| \approx 1\times10^{-6}$ cm^4 V^{-3} s^{-1}.

Graphene has been found to be one of the materials with the highest THz nonlinearity [12]. Since Hafez *et al.* reported directly the third-order nonlinear susceptibility $\chi^{(3)}(\omega+\omega+\omega\rightarrow3\omega)$, Eq. (4) immediately provides the nonlinear mobility $|\mu^{(3)}(\omega+\omega+\omega\rightarrow3\omega)| \approx 1.7\times10^{-6}$ cm^4 V^{-3} s^{-1}. The carrier density N due to doping was estimated as the ratio of graphene *sheet* carrier density and graphene thickness, these values being both indicated in Ref. [12].

The maximum nonlinear mobility (a measure of nonlinearity per unit charge) due to charge confinement is thus more than 20 times stronger than that in graphene, and ∼40 times stronger than the nonlinearity caused by intervalley scattering in GaAs. Since only the nanobar width has been optimized so far, there is a large potential for a further improvement of the strength of the confinement induced nonlinearity.

III. THZ WAVE INTERACTION WITH NONLINEAR MEDIUM

It is experimentally easy to probe the effective conductivity or photoconductivity of semiconductor nanostructures by free-space propagating THz radiation. However, the actual interpretation of such measurements is complicated due to the presence of depolarization fields which screen the incident THz pulse: These imply that the measured (effective) response differs from the microscopic response of the nanostructures. For the description of the *linear* response, several equivalent approaches (description in terms of plasmon formation, local field effects or effective medium approach) have been developed [18–20]; these currently constitute a well-known basis for the description of the propagation of electromagnetic waves in inhomogeneous media, which enables interpretation of the measured signals. However, the relation between the *nonlinear* response and nonlinear signals measured by THz spectroscopy in inhomogeneous systems has not been examined so far.

Here we will employ the effective medium approach based on the brick-wall effective medium approximation which allows a straightforward illustrative interpretation of the obtained formulas. Similarly as in the case of the linear inhomogeneous media, the task is split into two parts:

(i) Homogenization of the (nonlinear) inhomogeneous medium. This means replacing the nanobar array [Fig. 1(a)] by a homogeneous layer with equivalent (effective) properties [Fig. 1(b)].

(ii) Solution of the (nonlinear) wave equation in the homogenized layer.

These two steps are tightly interconnected in nonlinear inhomogenous media: the interaction of the electromagnetic wave depends on its intensity inside the nanobars while the determination of this intensity requires knowledge of both wave propagation through the structure and the homogenization procedure.

To simplify the task as much as possible, we will always consider a small signal limit. By this we man that:

(i) The electric field resulting from any nonlinear interaction is weak compared to the amplitude of the incident wave.

(ii) The nonlinear interactions do not deplete the driving wave.

These conditions assure that the nonlinearities do not cause a significant redistribution of the driving electric field, and therefore it is legitimate to decouple the description of the propagation of the incident wave (which is thus governed solely by the *linear* wave equation combined with *linear* effective medium theory) from the generation of the nonlinear signal.

In the following paragraphs, we will thus describe how the incident driving wave with electric field E_{inc} propagates in the sample. Using linear theories, we will determine the effective field E_{eff} in the equivalent homogenized layer, which then provides the driving electric field E inside the nanobars (Fig. 1). Subsequently, nonlinear effective medium theory will

be adapted to link the effective conductivity $\Delta\sigma^{(3)}_{\rm eff}$ of the equivalent homogenized layer to the nonlinear conductivity of the nanobars $\Delta\sigma^{(3)}$. Next, we will describe the propagation of the third-harmonic frequency generated in this homogenized nonlinear layer. The calculated intensity of the third harmonics leaving the sample will finally constitute the signal which can be directly compared with experiments.

In the calculations, we will additionally assume that the nanobar layer is optically thin (compared to the THz wavelengths of ∼0.3 mm) so that all internal reflections sum up without any significant phase shift. The calculations also aim to reproduce optical pump-THz probe experiments in which the linear and nonlinear conductivity $\Delta\sigma$ is induced by the excitation pulse. In order to reduce excessive math, we present only the most important formulas in the main text while detailed derivations are moved to appendices.

A. Propagation of the driving wave

When a wave with amplitude $E_{\rm inc}$ irradiates an optically thin homogeneous layer on a substrate at normal incidence [Fig. 1(b)], a standing wave with amplitude

$$E_{\rm eff}(\omega) = E_{\rm inc}(\omega)\frac{2}{1+n_{\rm sub}(\omega)} = E_{\rm T} \tag{11}$$

is generated in the thin layer (Appendix B). The fraction accounts for Fresnel reflection losses and interferences inside the optically thin sample attached to the substrate. In the following illustrations we will assume a sapphire substrate, which has refractive index $n_{\rm sub} \approx 3$; the fraction thus becomes $\sim\frac{1}{2}$. This order of magnitude is representative for most substrates transparent in the THz range. Note also that the amplitude $E_{\rm T}$ of the wave transmitted through the thin film is equal to $E_{\rm eff}$ [Eqs. (B1) and (B2)].

We introduce a factor Q which describes how the field E inside the individual nanobars is enhanced compared to the field $E_{\rm eff}$ in the equivalent homogenized layer,

$$E(\omega) = Q(\omega)E_{\rm eff}(\omega). \tag{12}$$

Within the brick-wall model [21–23] it is easy to show (Appendix C) that

$$Q(\omega) = \frac{\varepsilon_{\rm h}}{s\varepsilon_{\rm h} + (1-s)\left(\varepsilon + \frac{i\Delta\sigma^{\rm L}}{\omega\varepsilon_0}\right)}, \tag{13}$$

where $s = a/L$ is the volume filling factor of nanobars, and $\varepsilon_{\rm h}$ is the (linear) permittivity of the material which embeds the nanobars with (linear) permittivity ε and linear photoconductivity $\Delta\sigma^{\rm L} = e_0 N\mu^{\rm L}$. Altogether, supplying the linear mobility $\mu^{\rm L}$ from the Monte Carlo calculations and combining these three equations provides the amplitude E of the driving field in the individual nanobars and the intensity of the transmitted fundamental harmonics.

B. Nonlinear effective medium approximation

As discussed in Appendix D, the effective conductivity $\Delta\sigma^{(3)}_{\rm eff}(\omega+\omega+\omega\to 3\omega)$ describing the generation of the third harmonics via the canonical process reads

$$\Delta\sigma^{(3)}_{\rm eff}(\omega+\omega+\omega\to 3\omega) = sQ^3(\omega)Q(3\omega)\Delta\sigma^{(3)}(\omega+\omega+\omega\to 3\omega). \tag{14}$$

The $Q^3(\omega)$ term describes the enhancement of the driving THz field inside the nanobars, whereas the $Q(3\omega)$ term reflects the propagation of the resulting third harmonics through the heterogeneous structure.

While the effective nonlinear photoconductivity is directly proportional to the nonlinear mobility [Eq. (2)], one should keep in mind that the dependence on the excitation density N is more complex as it appears also in the field enhancement factors $Q(\omega)$ and $Q(3\omega)$. In the linear case, this dependence of $Q(\omega)$ leads to the blue shift of the plasmons [18].

C. THz wave propagation in nonlinear medium

The amplitude of the electric field ΔE of a wave generated by a surface current density $\Delta J_{\rm eff}$ in a homogeneous optically thin layer at an interface between air and a substrate with refractive index $n_{\rm sub}$ reads (e.g., the Appendix in Ref. [18])

$$\Delta E = -\frac{Z_0}{1+n_{\rm sub}}\Delta J_{\rm eff}, \tag{15}$$

where Z_0 is the vacuum impedance.

In our case, the surface current density $\Delta J_{\rm eff}$ is an integral of the nonlinear effective current density over the thickness of the nanostructure,

$$\Delta J_{\rm eff}(3\omega) = \int \Delta j_{\rm eff}(3\omega)dz = \int \frac{3}{4}\Delta\sigma^{(3)}_{\rm eff}(\omega+\omega+\omega\to 3\omega)E^3_{\rm eff}(\omega)dz. \tag{16}$$

The only quantity which is potentially dependent on the depth z inside the layer is the carrier density N entering through Eqs. (14) and (2) and also through the field enhancement factors Q. In order to avoid a heavy mathematical analysis (leading to complex expressions even in linear inhomogeneous media [24]), we adopt here the approximation that carriers are distributed in the nanobar layer homogeneously. If each photon is absorbed and generates an electron-hole pair, the integral $\int N(z)dz$ reduces to the excitation photon fluence F (number of photons in a laser pulse per unit area). The assumption of a homogeneous distribution is well justified in high-mobility semiconductors like GaAs or InP where diffusion homogenizes the initially inhomogeneous carrier population on the picosecond timescale [25].

Altogether, the sheet current density responsible for the generation of the third harmonics reads

$$\Delta J_{\rm eff}(3\omega) = \frac{s}{4}Q^3(\omega)Q(3\omega)e_0F\mu^{(3)} \times(\omega+\omega+\omega\to 3\omega)E^3_{\rm eff}(\omega). \tag{17}$$

In the experiments, the spectra ΔE are usually normalized by the complex amplitude $E_{\rm T}$ of the wave transmitted through the nonphotoexcited sample. This relative strength of the third-harmonic generation in the small signal limit constitutes

an important output of this paper:

$$\frac{\Delta E^{\mathrm{NL}}(3\omega)}{E_{\mathrm{T}}(\omega)} = -\frac{Z_0 e_0 F}{[1+n_{\mathrm{sub}}(\omega)]^3} s Q^3(\omega) Q(3\omega) \times E_{\mathrm{inc}}^2(\omega)\mu^{(3)}(\omega+\omega+\omega\to 3\omega), \quad (18)$$

which can be compared with experimental results.

D. Discussion

The relative signal strength [Eq. (18)] is controlled by the morphology of the structure, which is encoded in the filling factor s and in the magnitude of the Q factors: These merge into $s|Q^4|$ when the dispersion of material properties is negligible. For low excitation fluences F, the photoconductivity does not alter the dielectric contrast between the nanobars and the host medium significantly (i.e., $|\frac{\Delta\sigma}{\omega\varepsilon_0}| \ll \varepsilon \approx 12$ in GaAs), which means that Q is almost independent of F and the third-harmonic signal [Eq. (18)] thus increases linearly with the excitation fluence F (Fig. 6). For high excitation fluences (i.e., $|\frac{\Delta\sigma}{\omega\varepsilon_0}| \gg \varepsilon$), the enhanced photoconductivity of the nanobars screens more the incident electric field; $|Q|$ is then proportional to $1/F$ and therefore the measurable signal (18) decreases with increasing excitation fluence as F^{-3}. The relative strength of the third-harmonic signal for incident field amplitude $E_{\mathrm{inc}} = 10$ kV/cm (Fig. 6) reaches at most 2×10^{-7} (-134 dB). Although this signal could be enhanced by increasing the incident field, it would still remain close to the sensitivity limit of common optical pump-THz probe setups (for illustration, a dynamic range of 100 dB was reached in Ref. [26] after 14 hours of data acquisition). The low value of the measurable signal essentially stems from Eq. (13), which reduces to $1/[(1-s)(\varepsilon + \frac{i\Delta\sigma}{\omega\varepsilon_0})]$ for $|\varepsilon| \gg |\varepsilon_{\mathrm{h}}|$; the amplitude of Q is thus very low ($\ll 1$) as a result of the high permittivity of semiconductors and it further decreases with increasing photoconductivity.

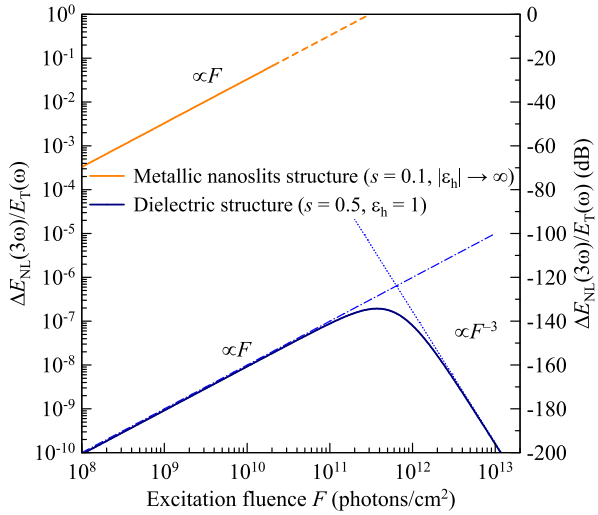

FIG. 6. Solid lines: The relative strength of the third-harmonic generation produced by a fundamental wave with frequency 0.5 THz with amplitude $E_{\mathrm{inc}} = 10$ kV/cm incident on the GaAs nanobar layer ($a = 250$ nm, $m_{\mathrm{eff}} = 0.07m_e$, $\tau_s = 270$ fs, room temperature) as a function of the excitation fluence, calculated using Eq. (18). The dashed style of the orange line emphasizes that Eq. (18) ceases to be valid for signals exceeding 10%.

A fundamental improvement of the measurable signal can be achieved using metallic nanoslits concentrating the electric field into the semiconductor [27,28]. In the presented formalism, the metal then plays the role of the host medium: its high conductivity implies a high permittivity magnitude (e.g., $|\varepsilon_{\mathrm{h}}| \approx |\frac{i\sigma_{\mathrm{h}}}{\omega\varepsilon_0}|$ in gold at 1 THz). As long as $s|\varepsilon_{\mathrm{h}}| \gg (1-s)|\varepsilon + i\Delta\sigma/(\omega\varepsilon_0)|$ (i.e., not an extremely low filling fraction or extremely high photoconductivity $\Delta\sigma$), the enhancement factor Q reduces to $1/s$ and the electric field E inside nanobars thus easily exceeds the incident one E_{inc} for low filling factors [27,28]. The third-harmonic signal is thus considerably enhanced and it remains proportional to the excitation fluence for a broad range of parameters (Fig. 6). The photoinduced nonlinear transmittance exceeds 10% (this level is the limit for which our theory built on the small signal limit is expected to remain valid) for excitation fluence $F = 3\times 10^{10}$ photons/cm^2, which can be generated even by a femtosecond laser oscillator. There is no principal obstacle for generating stronger nonlinear signals; a reasonable theoretical description (like finite-difference time-domain numerical calculations [29]) should additionally include namely the depletion of the driving field on conversion into higher harmonics.

The observed excitation fluence dependence (Fig. 6) for nanobars embedded in a dielectric material is analogous to the linear response of photoexcited inhomogeneous systems [20]. The nanobars in the dielectric structure do not form a percolation pathway, therefore the photoinduced effective response becomes limited by the capacitive reactance of the dielectric host medium above a certain level of nanobar photoconductivity. Conversely, the nanobars in metallic nanoslits are effectively percolated by the conducting metallic parts, therefore their effective photoconductivity scales linearly with the photoconductivity of the nanobars under common conditions.

E. Limitations

Semiclassical calculations of linear response of charges confined in semiconductor nanostructures accurately capture the physics for nano-object sizes exceeding tens of nanometers; quantum effects such as discrete quantum transitions start to play role only for smaller sizes or lower temperatures [30]. Since nanobars optimized for a strong nonlinear terahertz response are much wider, we believe that the semiclassical approach should be safely valid. We also neglected the THz-field-induced intervalley scattering which decreases the mobility of charges due to their scattering into side valleys with higher effective mass [10]. Nevertheless, this influence should be minor as the corresponding nonlinearity is much weaker than that due to the confinement (Sec. II D).

For practical realization, an additional insulating layer should separate the semiconductor nanobars from the metal to keep the charges confined in the nanobars and to suppress a band bending. We verified that even a 5-nm-thick insulating layer of a high-permittivity material such as TiO_2 does not compromise the outcome of the effective medium approximation employed in this letter and the response of the structure is thus still described by Eq. (18).

Strictly speaking, Eq. (18) provides the signal just after thin photoconducting layer. The fields on the left-hand side of Eq. (18) involve different frequency ranges and therefore the instrumental functions do not cancel out from the measured signals as in the case of linear spectroscopy [31]. A quantitative analysis of the experimentally measured signals thus should consider the detector response function together with spectral reshaping due to spatiotemporal transformations on propagation through focusing optics [32,33] or other dispersive elements. Furthermore, the signal [Eq. (18)] still involves the profile of the incident wave E_{inc}, which should also be determined to permit quantitative analysis.

IV. SUMMARY

Monte Carlo calculations of charge motion driven by an intense oscillating electric field have been developed to calculate the generalized nonlinear mobility spectra $\mu^{[\alpha]}(\alpha\omega)$ (representing the normalized amplitude of the charge velocity oscillations at frequency $\alpha\omega$ induced by a frequency ω) and the nonlinear mobility spectra $\mu^{(n)}$ analogical to the nonlinear susceptibility $\chi^{(n)}$ in optics. The nonlinear response of confined charges including efficient high-harmonic generation occurs even for moderate driving electric fields. Although the third-order nonlinear coefficient in optimum-sized nanobars is more than 20 times stronger than in graphene (one of the most nonlinear terahertz materials known so far), the nonlinear terahertz signal produced by isolated nano-objects is fundamentally suppressed due to the screening of the incident electric field by depolarization fields, and it is thus too weak to be observed experimentally. The full potential of the strong confinement-induced nonlinearity can be fully exploited on embedding the nano-objects into metallic nanoslits: the concentration of the field into the semiconductor easily generates a nonlinear photoinduced terahertz signal comparable with the linear-response signal. This paves a way toward exploitation of terahertz nonlinearities using existing sources delivering only moderate intensities of the terahertz radiation.

ACKNOWLEDGMENTS

We acknowledge the financial support by the Czech Science Foundation (Project No. 19-28375X) and by Operational Program Research, Development and Education financed by European Structural and Investment Funds and the Czech Ministry of Education, Youth and Sports (Project No. SOLID21–CZ.02.1.01/0.0/0.0/16/019/0000760). We also acknowledge Petr Kužel for fruitful discussions.

APPENDIX A: COMPLEX SPECTRA OF GENERALIZED MOBILITIES

In Fig. 7 we illustrate the real and imaginary parts of the generalized mobilities $\mu^{[\alpha]}$ corresponding to the amplitudes shown previously in Fig. 2. These spectra are linear combinations [Eq. (7)] of nonlinear mobilities $\mu^{(n)}$, which exhibit a rather complex shape themselves (Sec. II D).

APPENDIX B: ELECTRIC FIELD INSIDE AN OPTICALLY THIN LAYER

Wave propagation inside a multilayered stack can be generally described using a transfer matrix method. The homogenized nanobar structure is optically thin, therefore the phases of the waves acquired during the propagation through this thin layer can be neglected. The conditions of continuity of tangential components of electric and magnetic fields (E and H, respectively) at both interfaces thus reduce to

$$\begin{aligned} E_{\mathrm{inc}} + E_{\mathrm{R}} &= E_{\mathrm{F}} + E_{\mathrm{B}} = E_{\mathrm{T}} \\ H_{\mathrm{inc}} - H_{\mathrm{R}} &= H_{\mathrm{F}} - H_{\mathrm{B}} = H_{\mathrm{T}}, \end{aligned} \tag{B1}$$

where the subscripts inc, R, and T refer to the incident, reflected and transmitted waves, respectively. The indices F and B represent the waves propagating forward and backward inside the thin film (Fig. 8). Since $H = \frac{n}{Z_0}E$, where n is the refractive index of the pertinent layer and Z_0 is the vacuum impedance, the set of Eqs. (B1) yields the total electric field

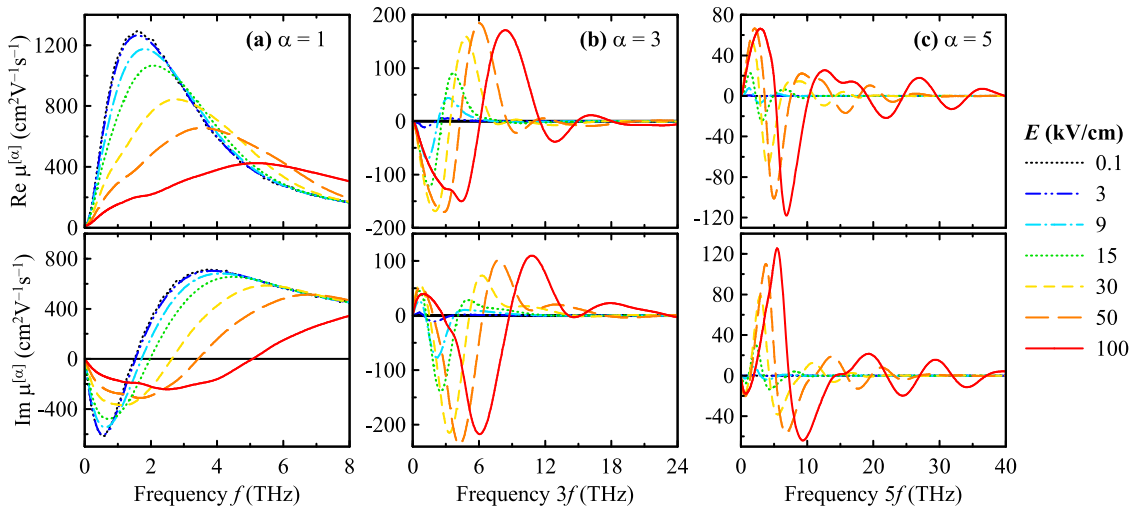

FIG. 7. Examples of the real and imaginary part of generalized mobilities $\mu^{[\alpha]}$ for 100-nm-wide GaAs nanobars ($m_{\mathrm{eff}} = 0.07m_e$, $\tau_s =$ 100 fs) at room temperature.

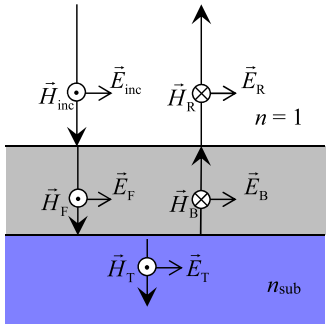

FIG. 8. Scheme of the propagation of the electromagnetic waves in a layered structure.

inside the thin layer (which is the field E_{eff} from Fig. 1)

$$E_{\text{F}} + E_{\text{B}} = \frac{2E_{\text{inc}}}{1 + n_{\text{sub}}}. \tag{B2}$$

Note that the electric field inside the thin layer is independent of its refractive index, which is a direct consequence of neglecting the propagator terms. An important implication is that the electric field inside the layer will remain the same when the layer is photoexcited.

APPENDIX C: LINEAR EFFECTIVE MEDIUM APPROXIMATION: BRICK-WALL MODEL

For THz electric field polarized perpendicularly to the nanobars (Fig. 1), the investigated nanobar array approximately behaves as an array of planar capacitors connected in series (e.g., Refs. [21–23]). Its effective permittivity without photoexcitation then follows the textbook formula

$$\varepsilon_{\text{eff}} = \frac{\varepsilon_{\text{h}}\varepsilon}{s\varepsilon_{\text{h}} + (1-s)\varepsilon}, \tag{C1}$$

where ε is the (linear) permittivity of the nanobars and ε_{h} is the permittivity of the material between the nanobars. On photoexcitation, the response of the nanobars changes due to the photoinduced conductivity to $\varepsilon + i\Delta\sigma^{\text{L}}/(\omega\varepsilon_0)$. The effective permittivity then changes from ε_{eff} to $\varepsilon_{\text{eff}} + i\Delta\sigma^{\text{L}}_{\text{eff}}/(\omega\varepsilon_0)$, where the photoinduced effective conductivity can be evaluated using (C1):

$$\Delta\sigma^{\text{L}}_{\text{eff}} = \Delta\sigma^{\text{L}} \frac{\varepsilon_{\text{h}}}{s\varepsilon_{\text{h}} + (1-s)\varepsilon} \frac{\varepsilon_{\text{h}}}{s\varepsilon_{\text{h}} + (1-s)\left(\varepsilon + \frac{i\Delta\sigma^{\text{L}}}{\omega\varepsilon_0}\right)}. \tag{C2}$$

The normal component of the displacement vector is preserved throughout the entire structure, i.e., $\varepsilon_{\text{eff}} E_{\text{eff},0} = \varepsilon E_0$ where $E_{\text{eff},0}$ is the (effective) electric field inside the homogenized layer and E_0 is the electric field inside the nanobar. We thus immediately obtain

$$\frac{E_0}{E_{\text{eff},0}} = \frac{\varepsilon_{\text{h}}}{s\varepsilon_{\text{h}} + (1-s)\varepsilon}. \tag{C3}$$

Analogically, the normal component of the displacement vector is preserved also on photoexcitation, i.e.,

$$\left(\varepsilon_{\text{eff}} + \frac{i\Delta\sigma^{\text{L}}_{\text{eff}}}{\omega\varepsilon_0}\right) E_{\text{eff}} = \left(\varepsilon + \frac{i\Delta\sigma^{\text{L}}}{\omega\varepsilon_0}\right) E. \tag{C4}$$

The field E inside a photoexcited nanobar thus becomes

$$\frac{E}{E_{\text{eff}}} = \frac{\varepsilon_{\text{h}}}{s\varepsilon_{\text{h}} + (1-s)\left(\varepsilon + \frac{i\Delta\sigma^{\text{L}}}{\omega\varepsilon_0}\right)} \equiv Q(\omega). \tag{C5}$$

We denote this expression as Q and its physical meaning is the enhancement of the electric field inside the nanobars, compared to the effective electric field in the homogenized layer.

For a later comparison between the linear and nonlinear effective response, it is interesting to notice that the transient effective conductivity can be elegantly expressed using the enhancement factors:

$$\Delta\sigma^{\text{L}}_{\text{eff}}(\omega) = sQ_0(\omega)Q(\omega)\Delta\sigma^{\text{L}}(\omega), \tag{C6}$$

where Q_0 is the enhancement factor without photoexcitation ($\Delta\sigma^{\text{L}} = 0$).

APPENDIX D: NONLINEAR EFFECTIVE MEDIUM APPROXIMATION

Recalling the linear Maxwell-Garnett mixing formula (e.g., Ref. [34])

$$\frac{\varepsilon_{\text{eff}} - \varepsilon_{\text{h}}}{\varepsilon_{\text{eff}} + K\varepsilon_{\text{h}}} = s\frac{\varepsilon - \varepsilon_{\text{h}}}{\varepsilon + K\varepsilon_{\text{h}}}, \tag{D1}$$

we realize that it coincides with the brick-wall model when we set $K = 0$. Nonlinear effective response within the Maxwell-Garnett approximation has been investigated extensively, e.g., in Refs. [35–37]. The key formula for our particular structure is Eq. (38) in Ref. [37], which was derived for dilute spherical inclusions (i.e., depolarization factor $K = 2$ and filling factor $s \ll 1$) and where we can ignore the second-order term due to the centrosymmetric character of our structure. In our notation, we thus start from the expression

$$\begin{aligned}\Delta\sigma^{(3)}_{\text{eff}}(\omega+\omega+\omega\to 3\omega) &= s\frac{3\varepsilon_{\text{h}}(3\omega)}{\varepsilon(3\omega)+2\varepsilon_{\text{h}}(3\omega)}\left[\frac{3\varepsilon_{\text{h}}(\omega)}{\varepsilon(\omega)+2\varepsilon_{\text{h}}(\omega)}\right]^3 \\ &\quad\times\Delta\sigma^{(3)}(\omega+\omega+\omega\to 3\omega),\end{aligned} \tag{D2}$$

which links the third-order nonlinear effective conductivity of the composite $\Delta\sigma^{(3)}_{\text{eff}}$ and the third-order conductivity of the nanobars $\Delta\sigma^{(3)}$. We need to generalize this relation for the nondilute limit and for a general depolarization factor K. This was to a large extent done in Eq. (5.8) in Ref. [35], which permits us to rewrite (D2) as

$$\begin{aligned}\Delta\sigma^{(3)}_{\text{eff}}(\omega+\omega+\omega\to 3\omega) &= s\frac{\varepsilon_{\text{eff}}(3\omega)+K\varepsilon_{\text{h}}(3\omega)}{\varepsilon(3\omega)+K\varepsilon_{\text{h}}(3\omega)}\left[\frac{\varepsilon_{\text{eff}}(\omega)+K\varepsilon_{\text{h}}(\omega)}{\varepsilon(\omega)+K\varepsilon_{\text{h}}(\omega)}\right]^3 \\ &\quad\times\Delta\sigma^{(3)}(\omega+\omega+\omega\to 3\omega).\end{aligned} \tag{D3}$$

Substituting for ε_{eff} from (D1), replacing the nanobar permittivity ε by the value on photoexcitation $\varepsilon + \frac{i\Delta\sigma^{\text{L}}}{\omega\varepsilon_0}$ and using the

definition of the field enhancement factor [Eq. (C5)], we thus obtain

$$\Delta\sigma_{\mathrm{eff}}^{(3)}(\omega+\omega+\omega\rightarrow 3\omega) = sQ^{3}(\omega)Q(3\omega)\Delta\sigma^{(3)}(\omega+\omega+\omega\rightarrow 3\omega). \quad \text{(D4)}$$

Unlike in (C2), all enhancement factors entering this equation correspond to the photoexcited state. The $Q^3(\omega)$ term describes the enhancement of the incident THz field inside the nanobars, whereas the $Q(3\omega)$ term reflects the propagation of the resulting third harmonics through the heterogeneous structure.

The development of nonlinear effective medium theories still remains an abundant field itself. The approach adapted here is thus inevitably highly simplified and we try to emphasize here just the most important behavior.

[1] R. W. Boyd, *Nonlinear Optics*, 3rd ed. (Academic Press, San Diego, CA, 2008).
[2] C. A. Schmuttenmaer, Chem. Rev. **104**, 1759 (2004).
[3] F. A. Hegmann, O. Ostroverkhova, and D. G. Cooke, Probing organic semiconductors with terahertz pulses, in *Photophysics of Molecular Materials* (Wiley-VCH Verlag GmbH & Co. KGaA, Weinheim, 2006), pp. 367–428.
[4] J. Lloyd-Hughes and T.-I. Jeon, Int. J. Infrared Millimeter Waves **33**, 871 (2012).
[5] P. Kužel and H. Němec, Adv. Opt. Mater. **8**, 1900623 (2020).
[6] J. Hebling, K.-L. Yeh, M. C. Hoffmann, B. Bartal, and K. A. Nelson, J. Opt. Soc. Am. B **25**, B6 (2008).
[7] B. Green, S. Kovalev, V. Asgekar, G. Geloni, U. Lehnert, T. Golz, M. Kuntzsch, C. Bauer, J. Hauser, J. Voigtlaender *et al.*, Sci. Rep. **6**, 22256 (2016).
[8] T. Kampfrath, K. Tanaka, and K. A. Nelson, Nat. Photon. **7**, 680 (2013).
[9] A. Leitenstorfer, K. A. Nelson, K. Reimann, and K. Tanaka, New J. Phys. **16**, 045016 (2014).
[10] J. Hebling, M. C. Hoffmann, H. Y. Hwang, K.-L. Yeh, and K. A. Nelson, Phys. Rev. B **81**, 035201 (2010).
[11] W. Kuehn, P. Gaal, K. Reimann, M. Woerner, T. Elsaesser, and R. Hey, Phys. Rev. B **82**, 075204 (2010).
[12] H. A. Hafez, S. Kovalev, J.-C. Deinert, Z. Mics, B. Green, N. Awari, M. Chen, S. Germanskiy, U. Lehnert, J. Teichert *et al.*, Nature (Lond.) **561**, 507 (2018).
[13] L. Brus, Appl. Phys. A **53**, 465 (1991).
[14] T. L. Cocker, D. Baillie, M. Buruma, L. V. Titova, R. D. Sydora, F. Marsiglio, and F. A. Hegmann, Phys. Rev. B **96**, 205439 (2017).
[15] H. Němec, P. Kužel, and V. Sundström, Phys. Rev. B **79**, 115309 (2009).
[16] J. Kuchařík, H. Němec, and T. Ostatnický, Phys. Rev. B **99**, 035407 (2019).
[17] R. C. Miller, Appl. Phys. Lett. **5**, 17 (1964).
[18] H.-K. Nienhuys and V. Sundström, Appl. Phys. Lett. **87**, 012101 (2005).
[19] E. Hendry, M. Koeberg, B. O'Regan, and M. Bonn, Nano Lett. **6**, 755 (2006).
[20] H. Němec, V. Zajac, I. Rychetský, D. Fattakhova-Rohlfing, B. Mandlmeier, T. Bein, Z. Mics, and P. Kužel, IEEE Trans. Terahertz Sci. Technol. **3**, 302 (2013).
[21] T. Ostapchuk, J. Petzelt, V. Železný, A. Pashkin, J. Pokorný, I. Drbohlav, R. Kužel, D. Rafaja, B. P. Gorshunov, M. Dressel *et al.*, Phys. Rev. B **66**, 235406 (2002).
[22] I. Rychetský and J. Petzelt, Ferroelectrics **333**, 227 (2006).
[23] C. Kadlec, F. Kadlec, P. Kužel, K. Blary, and P. Mounaix, Opt. Lett. **33**, 2275 (2008).
[24] P. Kužel and H. Němec, J. Phys. D **47**, 374005 (2014).
[25] C. S. Ponseca, Jr., H. Němec, J. Wallentin, N. Anttu, J. P. Beech, A. Iqbal, M. Borgström, M.-E. Pistol, L. Samuelson, and A. Yartsev, Phys. Rev. B **90**, 085405 (2014).
[26] H. Němec, I. Kratochvílová, P. Kužel, J. Šebera, A. Kochalska, J. Nožár, and S. Nešpůrek, Phys. Chem. Chem. Phys. **13**, 2850 (2011).
[27] H. Merbold, A. Bitzer, and T. Feurer, Opt. Express **19**, 7262 (2011).
[28] A. Novitsky, A. M. Ivinskaya, M. Zalkovskij, R. Malureanu, P. U. Jepsen, and A. V. Lavrinenko, J. Appl. Phys. **112**, 074318 (2012).
[29] L. Yang, J. Tian, K. Z. Rajab, and Y. Hao, IEEE Antennas Wirel. Propag. Lett. **17**, 126 (2018).
[30] T. Ostatnický, V. Pushkarev, H. Němec, and P. Kužel, Phys. Rev. B **97**, 085426 (2018).
[31] L. Duvillaret, F. Garet, and J.-L. Coutaz, IEEE J. Sel. Top. Quant. Electron. **2**, 739 (1996).
[32] D. You and P. H. Bucksbaum, J. Opt. Soc. Am. B **14**, 1651 (1997).
[33] P. Kužel, M. A. Khazan, and J. Kroupa, J. Opt. Soc. Am. B **16**, 1795 (1999).
[34] H. Němec, P. Kužel, and V. Sundström, J. Photochem. Photobiol. A **215**, 123 (2010).
[35] J. E. Sipe and R. W. Boyd, Phys. Rev. A **46**, 1614 (1992).
[36] P. M. Hui and D. Stroud, J. Appl. Phys. **82**, 4740 (1997).
[37] P. M. Hui, P. Cheung, and D. Stroud, J. Appl. Phys. **84**, 3451 (1998).